INSTITUTE OF PHYSICS PUBLISHING SMART MATERIALS AND STRUCTURES
Smart Mater. Struct. **10** (2001) 819–833 PII: S0964-1726(01)26511-2

Ionic polymer–metal composites: I. Fundamentals

Mohsen Shahinpoor[1,2,3] **and Kwang J Kim**[1,2]

[1] Artificial Muscle Research Institute, School of Engineering and School of Medicine, The University of New Mexico, Albuquerque, NM 87131, USA
[2] Environmental Robots, Inc., Albuquerque, NM 87108, USA

Received 3 January 2001, in final form 22 March 2001
Published 7 August 2001
Online at stacks.iop.org/SMS/10/819

Abstract
This paper, the first in a series of four review papers, presents a brief summary of the fundamental properties and characteristics of ionic polymeric–metal composites (IPMCs) as biomimetic sensors, actuators and artificial muscles. The forthcoming three review papers, to follow this paper, will address in detail such fundamentals and, in particular, manufacturing techniques and the electronic and electromechanical characteristics of IPMCs (part II), the phenomenological modelling of the underlying sensing and actuation mechanisms in IPMCs (part III) and the potential application areas for IPMCs (part IV). This paper is a summary of all recent findings and current state-of-the art manufacturing techniques, phenomenological laws and mechanical and electrical characteristics. A number of methodologies in developing high-force-density IPMCs are also reported.

(Some figures in this article are in colour only in the electronic version)

1. Ionic polymer–metal composites—in general

It is now well documented [1–7] that ionic polymers in a composite form with a conductive medium such as a metal (herein called ionic polymer–metal composites, IPMCs) can exhibit large dynamic deformation if suitably electroded and placed in a time-varying electric field (see figure 1). Conversely, dynamic deformation of such ionic polymers produces dynamic electric fields across their electrodes as shown in figure 2. A recently presented model by de Gennes *et al* [7] describes the underlying principle of electro-thermodynamics in such ionic polymers based upon internal transport phenomena and electrophoresis. IPMCs show great potential as soft robotic actuators, artificial muscles and dynamic sensors in the micro-to-macro size range. In this paper, the fundamentals of IPMCs with regard to their manufacturing techniques, phenomenological laws and electronic and electromechanical characteristics are presented.

Manufacturing of an IPMC starts with an ionic polymer with ion exchanging capability which is then chemically treated with an ionic salt solution of a metal and then chemically reduced to yield ionic polymer metal composites. The term *ion exchange polymers* refers to polymers designed to selectively exchange ions of a single charge (either cations or anions) with their own incipient ions. They are often manufactured from polymers that consist of fixed covalent ionic groups. Typical ion exchange polymers are the following.

(i) Perfluorinated alkenes with short side-chains terminated by ionic groups (typically sulfonate or carboxylate (SO_3^- or COO^-) for cation exchange or ammonium cations for anion exchange (see figure 3)). The large polymer backbones determine their mechanical strength. Short side-chains provide ionic groups that interact with water and the passage of appropriate ions.

(ii) Styrene/divinylbenzene-based polymers in which the ionic groups have been substituted from the phenyl rings where the nitrogen atom is fixed to an ionic group. These polymers are highly crosslinked and are rigid.

In perfluorinated sulfonic acid polymers there are relatively few fixed ionic groups. They are located at the end of side-chains so as to position themselves in their preferred orientation to some extent. Therefore, they can create hydrophilic nano-channels, so-called *cluster networks*. Such configurations are completely different in other ionic polymers such as styrene/divinylbenzene families that are primarily limited by crosslinking, the ability of the ionic polymers to expand (due to their hydrophilic nature).

[3] Corresponding author.

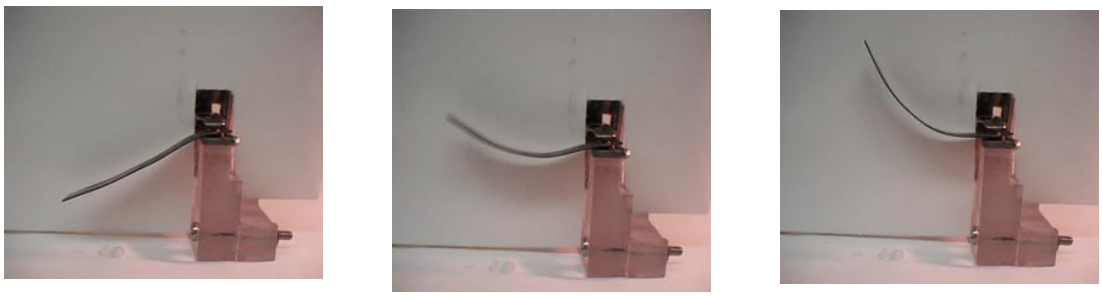

Figure 1. Successive photographs of an IPMC strip that shows very large deformation (up to 4 cm) in the presence of low voltage. Note that $\Delta t = 0.5$ s, 2 V applied. The sample is 1 cm wide, 4 cm long and 0.2 mm thick.

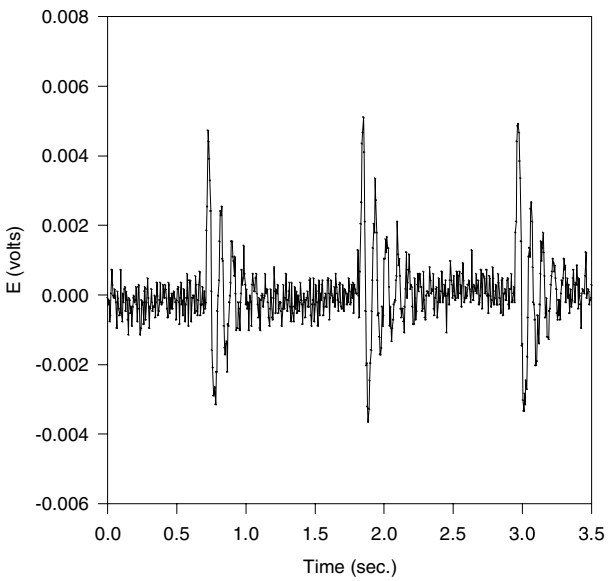

Figure 2. A typical sensing response of an IPMC. It shows the dynamic sensing response of a strip of an IPMC (a thickness of 0.2 mm) subject to a dynamic impact loading in a cantilever configuration. A damped electric response is observed, which is highly repeatable with a high bandwidth of up to 100 Hz. Such direct mechanoelectric behaviours are related to the endo-ionic mobility due to imposed stresses. This implies that, if we impose a finite solvent (= water) flux, $|Q|$, not allowing a current flux, $J = 0$, a certain conjugate electric field, $\vec{E}$, is produced that can be dynamically monitored as discussed later in section 3.

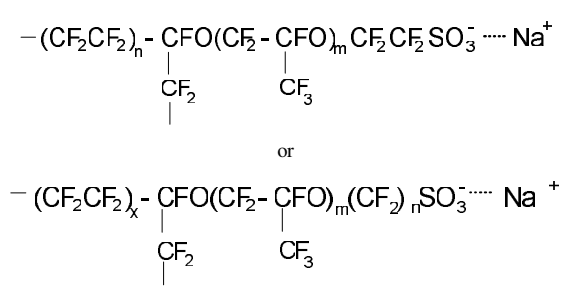

Figure 3. Perfluorinated sulfonic acid polymers. The counter-ion, Na^+ in this case, can simply be replaced by other ions.

2. Manufacturing techniques

The preparation of ionic polymer–metal composites (IPMCs) requires involved laboratory work. The current state-of-the-art IPMC manufacturing technique [4–6] incorporates two distinct preparation processes: first the *initial compositing process* and then the surface electroding process. Due to different preparation processes, morphologies of precipitated platinum are significantly different. Figure 4 shows illustrative schematic diagrams of two different preparation processes (top left and bottom left) and two top-view SEM micrographs for the platinum surface electrode (top right and bottom right).

The initial compositing process requires an appropriate metal salt such as $Pt(NH_3)_4HCl$ in the context of chemical reduction processes. These processes are similar to the processes evaluated by a number of investigators including Takenaka *et al* [8] and Millet *et al* [9]. The principle of the compositing process is to metallize the inner surface of the polymer by a chemical-reduction means such as $LiBH_4$ or $NaBH_4$. The ionic polymer is soaked in a salt solution to allow platinum-containing cations to diffuse through via the ion-exchange process. Later, a proper reducing agent such as $LiBH_4$ or $NaBH_4$ is introduced to metallize the polymer [10]. As can be seen in figure 5, the metallic platinum particles are not homogeneously formed across the membrane but concentrate predominantly near the interface boundaries. It has been experimentally observed that the platinum particulate layer is buried microns deep (typically 1–20 μm) within the IPMC surface and is highly dispersed. The fabricated IPMCs can be optimized to produce a maximum force density by changing multiple process parameters. These parameters include time-dependent concentrations of the salt and the reducing agents (applying the Taguchi technique to identify the optimum process parameters has proved quite attractive [11]). The primary reaction for platinum composites is

$$LiBH_4 + 4[Pt(NH_3)_4]^{2+} + 8OH^- \Rightarrow 4Pt^o + 16NH_3 + LiBO_2 + 6H_2O. \quad (1)$$

In the subsequent surface electroding process, multiple reducing agents are introduced (under optimized concentrations) to carry out the reducing reaction similar to equation (1), in addition to the initial platinum layer formed by the initial compositing process. This is clearly shown in figure 4 (bottom right), where the roughened surface disappears. In general, the majority of platinum salts stays in the solution and precedes the reducing reactions and production of platinum metal. Other metals (or conducting media), which are also successfully used, include palladium, silver, gold, carbon, graphite and nanotubes.

To characterize the surface morphology of the IPMC atomic force microscopy (AFM) can be used. Its capability to directly image the surface of the IPMC can provide detailed

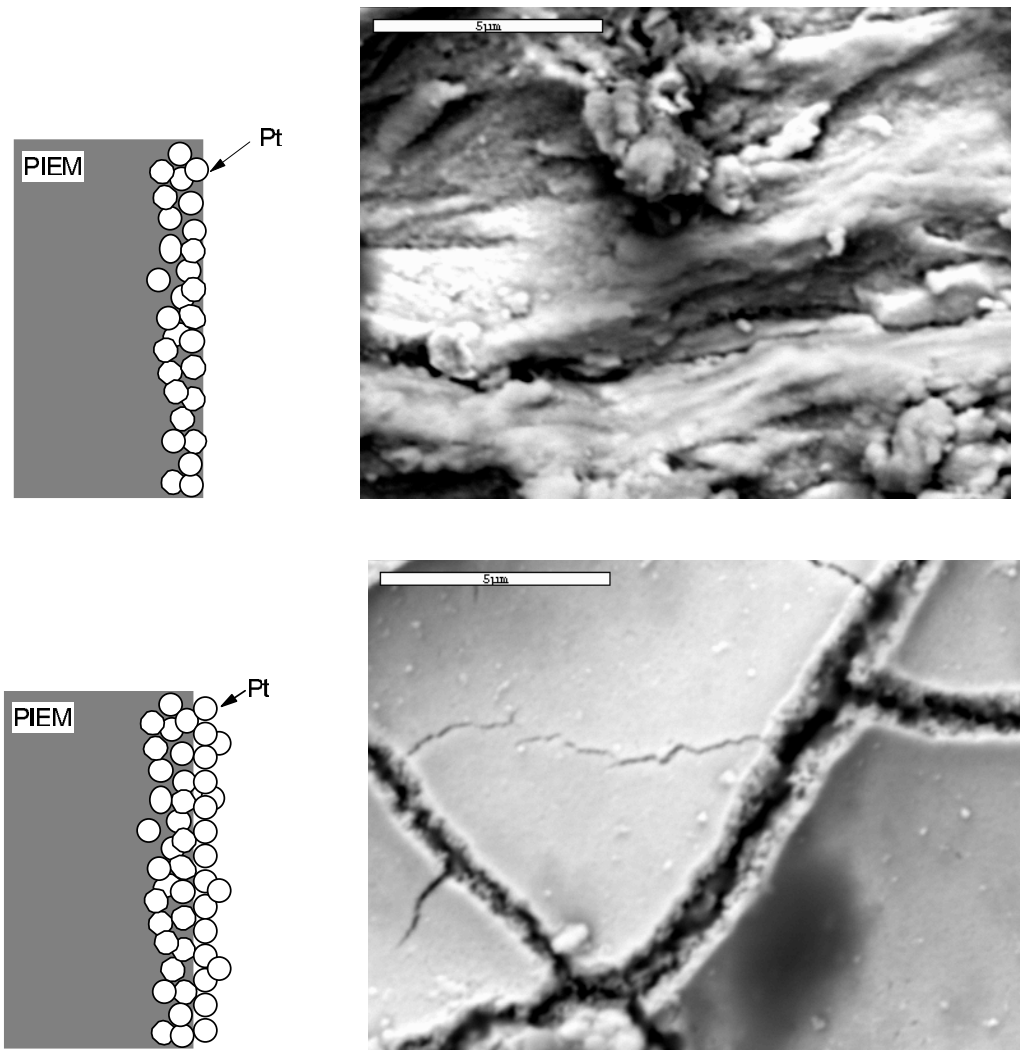

Figure 4. Two schematic diagrams showing different preparation processes: top left, a schematic diagram shows the initial compositing process; top right, its top-view SEM micrograph; bottom left, a schematic diagram shows the surface electroding process, and bottom right, its top-view SEM micrograph, where platinum has deposited predominately on top of the initial Pt layer. Note that PIEM stands for perfluorinated ion exchange membrane.

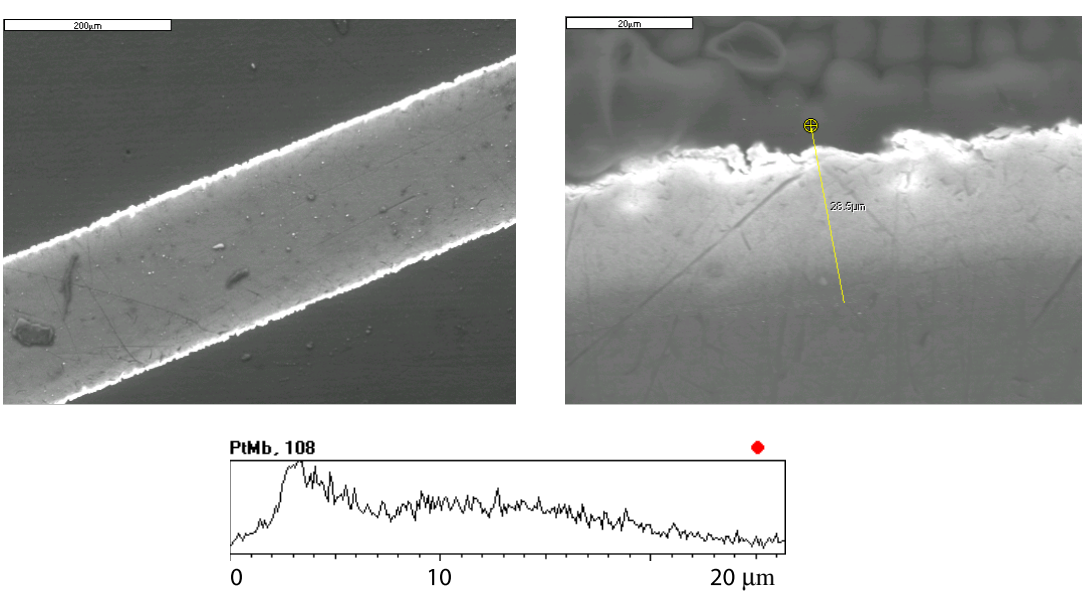

Figure 5. Two SEM micrographs (top) showing the cross-section (left) and close-up (right) of a typical IPMC. The bottom graph shows an x-ray line scan of Pt. As can be noticed, Pt is dense at the surface.

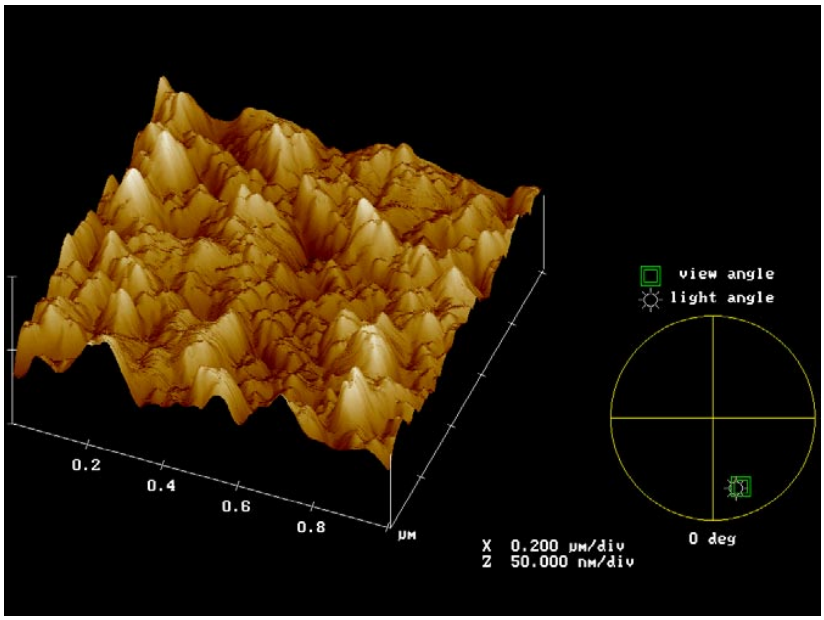

Figure 6. An AFM surface analysis image taken on the surface electrode of a typical muscle shown in figure 4 (bottom-right). The scanned area is 1 μm^2. The brighter/darker area corresponds to a peak/valley depth of 50 nm. The surface analysis image has a view angle set at 22°. Digital Instruments' AFM NanoScope IIIa was used. A tip (ultra levers) from Park Scientific Instrument was utilized in an air-contact mode under low voltage.

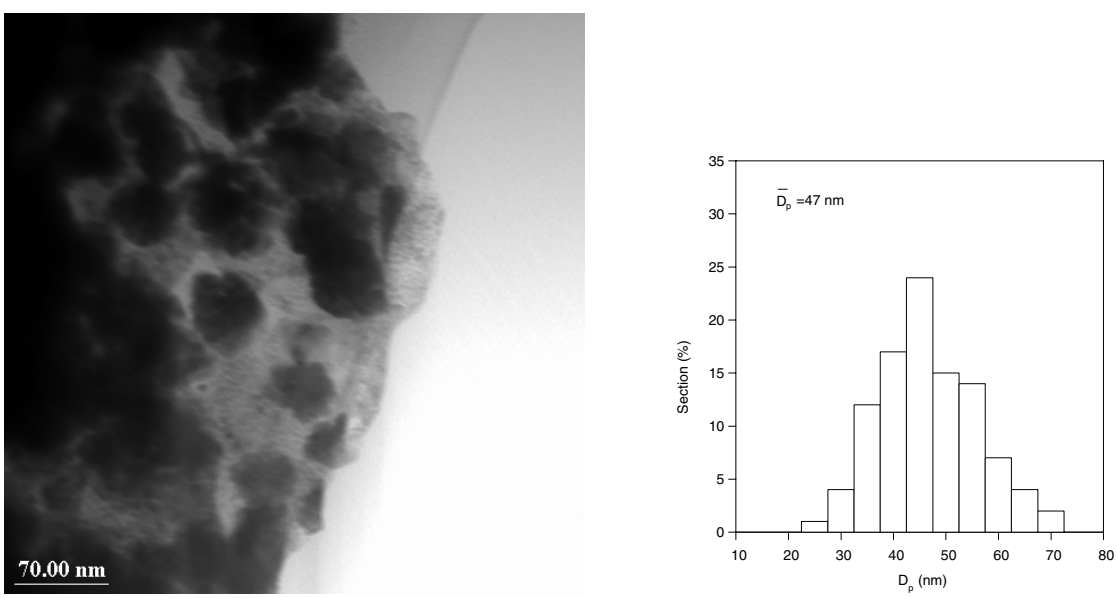

Figure 7. A TEM micrograph of the IPMC. It is on the penetrating edge of the IPMC. The sample was carefully prepared in a small piece and ion-beam treated.

information with a resolution of a few nanometres. In figure 6 a representative AFM image (its surface analysis) is presented that reveals the surface morphology of the IPMC. As can be seen, the surface is characterized by the granular appearance of platinum metal with a peak/valley depth of approximately 50 nm. This granular nano-roughness is responsible for producing a high level of electric resistance, yet provides a porous layer that allows water movement in and out of the membrane. During the AFM study, it was also found that platinum particles are dense and, to some extent, possess coagulated shapes. Therefore, the study was extended to utilize TEM, to determine the size of the deposited platinum particles. Figure 7 shows a TEM image on the penetrating edge of the IPMC. The sample was carefully prepared in the form of a small piece and was ion-beam treated. The average particle size was found to be around 47 nm.

3. Phenomenological law

A recent study by de Gennes *et al* [7] has presented the standard Onsager formulation on the underlining principle of IPMC actuation/sensing phenomena using linear irreversible thermodynamics: when static conditions are imposed, a simple description of the *mechanoelectric effect* is possible based

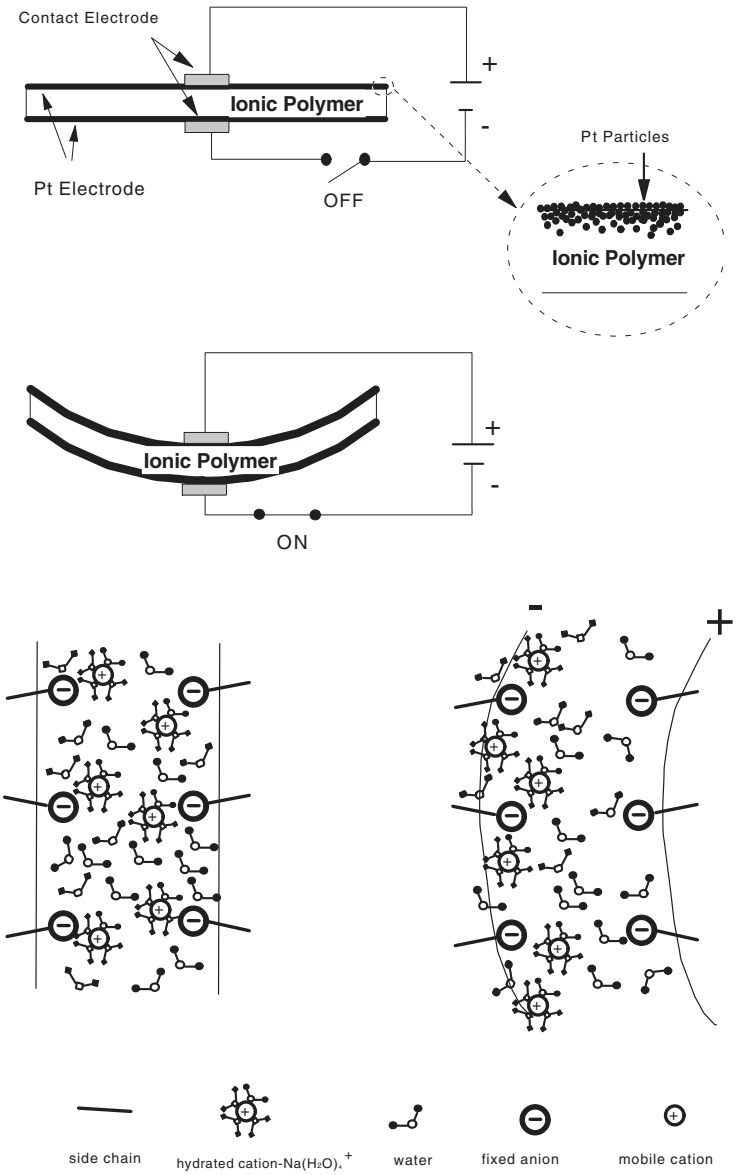

Figure 8. A schematic diagram of the typical IPMC artificial muscle and its actuation principle. The IPMC is composed of a perfluorinated ionic polymer, which is chemically surface composited with a conductive medium such as platinum. A platinum layer is formed a few microns deep within the perfluorinated ionic polymer. Typically, the strip of the perfluorinated ionic polymer membrane bends toward the anode (in the case of cation exchange membranes) under the influence of an electric potential. Also, the appearance of water on the surface of the expansion side and the disappearance of water on the surface of the contraction side are common. This electrophoresis-like internal ion–water movement is responsible for creating effective strains for actuation. Water leakage through the porous Pt electrode reduces the electromechanical conversion efficiency.

upon two forms of transport: *ion transport* (with a current density, J, normal to the material) and *electrophoretic solvent transport* (with a flux, Q; we can assume that this term is water flux). The conjugate forces include the electric field, $\vec{E}$, and the pressure gradient, $-\nabla p$. The resulting equation has the concise form of

$$J = \sigma \vec{E} - L_{12} \nabla p, \tag{2}$$

$$Q = L_{21} \vec{E} - K \nabla p, \tag{3}$$

where σ and K are the membrane conductance and the Darcy permeability, respectively. The cross-coefficient is usually $L_{12} = L_{21} = L$, experimentally measured to be of the order of 10^{-8} $((\mathrm{m\ s^{-1}})/(\mathrm{V\ m^{-1}}))$. The simplicity of the above equations provides a compact view of underlining principles of both actuation and sensing of the IPMC. So, we can illustrate it simply in figure 8.

4. Characteristics

Mechanical. Figure 9 shows tensile testing results, in terms of normal stress versus normal strain, on a typical IPMC (H^+ form) relative to Nafion^{TM}-117 (H^+ form). Recognizing that Nafion^{TM}-117 is the adopted starting material for this IPMC, this comparison is useful. There is a little increase in mechanical strength of IPMC (both stiffness and the modulus of elasticity), but it still follows the intrinsic nature of Nafion itself. This means that, in tensile (positive) strain,

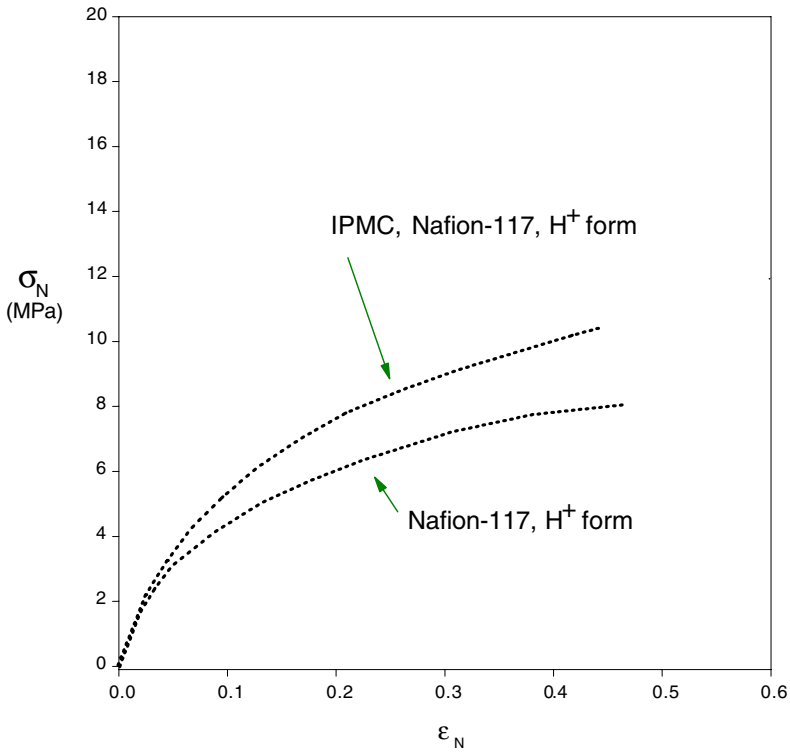

Figure 9. Tensile testing results. Normal stress, σ_N, versus normal strain, ε_N; IPMC and Nafion-117^{TM}. Note that both samples were fully hydrated when they were tested.

the stress/strain behaviour is predominated by the polymer material rather than metallic powders (composited electrode materials).

Although the tensile testing results show the intrinsic nature of the IPMC, a problem arises when the IPMC operates in a bending mode. Dissimilar mechanical properties of the metal particles (the electrode) and polymer network seem to affect each other. Therefore, in order to construct the effective stress–strain curves for IPMCs, strips of IPMCs are suitably cut and tested in a cantilever configuration (see figure 10(*a*)). In a cantilever configuration, the end deflection δ due to a distributed load $w(s, t)$, where s is the arc length of a beam of length L and t is the time, can be related approximately to the radius of curvature ρ of the bent cantilever beam, i.e.

$$\rho \cong \frac{L^2 + \delta^2}{2\delta}. \tag{4}$$

Note that the radius of curvature ρ is in turn related to the maximum tensile (positive) or compressive (negative) strains in the beam as

$$\varepsilon \cong \frac{h}{2\rho}, \tag{5}$$

where h is the thickness of the beam at the built-in end. Note that in the actuation mode of the IPMC, the tensile strain can be simply realized, but difficult to isolate. In the negative strain (material compression) illustrated in figure 10(*b*), the metal particles become predominant so as to create much higher stiffness and modulus of elasticity than the ones in the positive-strain regime. Thus, the mathematical description regarding the granular physics of the cantilever beam of the IPMC should be addressed. Experimental approaches are also available and should be pursued.

The stress σ can be related to the strain ε by simply using Hooke's law, assuming linear elasticity (one can also consider other constitutive equations in which the stress σ can be related to the strain ε in a nonlinear fashion (i.e. rubber elasticity—this could be a future study)). It leads to

$$\sigma = \frac{Mh}{2I}, \tag{6}$$

where σ is the stress tensor, M is the maximum moment at the built-in end and I is the moment of inertia of the cross-section of the beam. Thus, the moment M can be calculated based on the distributed load on the beam or the applied electrical activation of the IPMC beam. Having also calculated the moment of inertia I, which for a rectangular cross-section of width b will be $I = bh^3/12$, the stress σ can be related to the strain ε and the representative results are plotted in figures 10(*c*) and (*d*). These figures include the effect of swelling (*c*) and stiffening behaviour under electric activation (*d*). Here, electric activation refers to the IPMC in the electro-mechanical mode exhibiting increased stiffness due to redistributed hydrated ions or nonlinear characteristics of electromechanical properties of the IPMC. These features will be discussed in detail in upcoming review papers.

Electrical. In order to assess the electrical properties of the IPMC, the standard ac impedance method that can reveal the equivalent electric circuit has been adopted. A typical measured impedance plot, provided in figure 11, shows the frequency dependence of impedance of the IPMC. It is interesting to note that the IPMC is nearly resistive (>50 Ω) in the high-frequency range and fairly capacitive (>100 μF) in the low-frequency range.

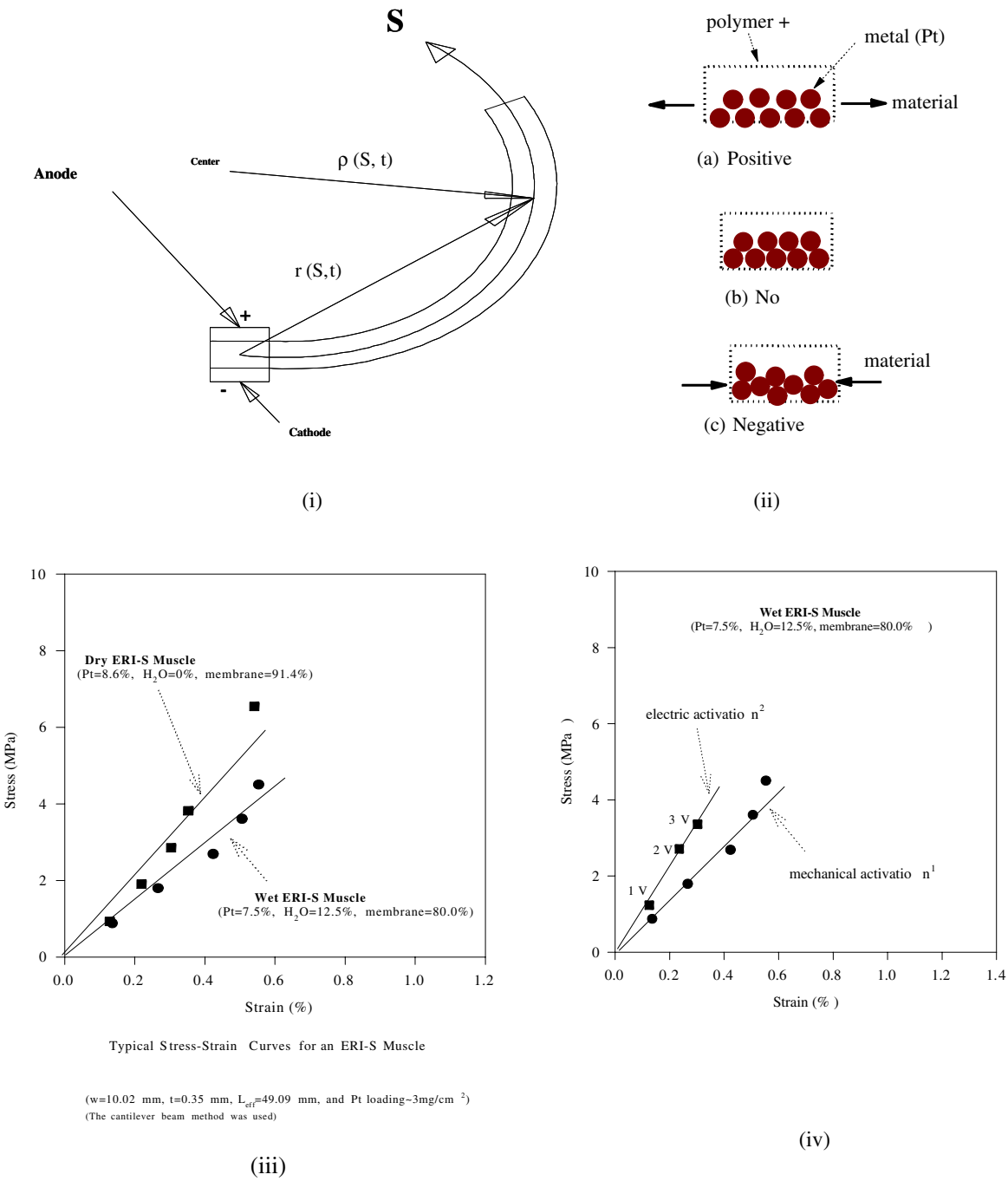

Figure 10. A cantilever configuration of the IPMC (*i*) and an illustration of positive/negative strains experienced in the operation mode of the IPMC (*ii*). The bottom graphs show the effect of swelling (*iii*) and stiffening behaviour under electric activation (*iv*). Swelling is also an important parameter to affect the mechanical property. Swelling causes mechanical weakening. Electric activation has a tendency to stiffen the material due to redistribution of ions within the IPMC.

Based upon the above findings, we consider a simplified equivalent electric circuit of a typical IPMC such as the one shown in figure 12 [6]. In this approach, each single unit circuit (i) is assumed to be connected in a series of arbitrary surface resistance (R_{ss}) in the surface. This approach is based upon the experimental observation of the considerable surface-electrode resistance (see figure 12). We assume that there are four components to each single unit circuit: the surface-electrode resistance (R_s), the polymer resistance (R_p), the capacitance related to the ionic polymer and the double layer at the surface-electrode/electrolyte interface (C_d) and an impedance (Z_w) due to a charge transfer resistance near the surface electrode. For the typical IPMC, the importance of R_{ss} relative to R_s may be interpreted from $\Sigma R_{ss}/R_s \approx L/t \gg 1$, where notations L and t are the length and thickness of the electrode, respectively. It becomes a two-dimensional electrode. In order to increase the surface conductivity, a thin layer of a highly conductive metal (such as gold) is deposited on top of the platinum surface electrode [6].

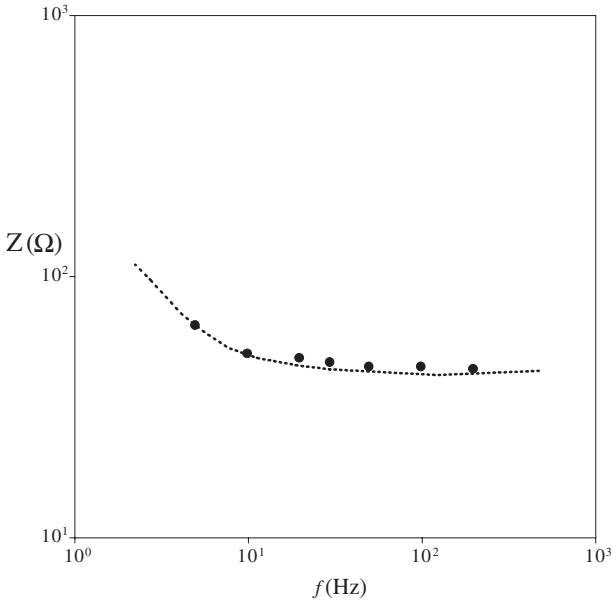

Figure 11. The measured ac impedance spectra (magnitude) of an IPMC sample. (The wet IPMC sample has dimensions of 5 mm width, 20 mm length and 0.2 mm thickness.)

Realizing that water contained in the perfluorinated IPMC network is the sole solvent that can create useful strains in the actuation mode, another issue to deal with is the so-called 'decomposition voltage'. As can be clearly seen in figure 13, the decomposition voltage is the minimum voltage at which significant electrolysis occurs. This figure contains the graph of steady-state current, I, versus applied dc voltage, E_{app}, showing that as the voltage increases, there is little change in current (obeying Faraday's law). However, a remarkable increase in dc current is observed with a small change of voltage. Even though the intrinsic voltage causing water electrolysis is about 1.23 V, a small overpotential (ca 0.3–0.5 V) was observed. It should be noted that such water electrolysis leads to lower thermodynamic efficiency of the IPMC.

Figure 14 depicts measured cyclic current/voltage responses of a typical IPMC (the scan rate is 100 mV s^{-1}). As can be seen, a rather simple behaviour with a small hysteresis is obtained. Note that the reactivity of the IPMC is mild, so that it does not show any distinct reduction or re-oxidation peaks within ±4 V, except for a decomposition behaviour at $\sim \pm 1.5$ V, where the extra current consumption is apparently due to electrolysis. The overall behaviour of the IPMC shows a simple trend of ionic motions caused under an imposed electric field.

In figure 15, the frequency dependence of the IPMC is expressed in terms of the normal stress versus the normal strain. Its frequency dependence shows that as frequency increases the beam displacement decreases. However, it must be realized that, at low frequencies (0.1–1 Hz), the effective elastic modulus of the IPMC cantilever strip under an imposed voltage is also rather small. On the other hand, at high frequencies (5–20 Hz) such moduli are larger and displacements are smaller. This is due to the fact that at low frequencies water and hydrated ions have time to gush out of the surface electrodes while at high frequencies they are rather contained inside the polymer. Therefore, the nature of water and hydrated ion transport within the IPMC can affect the moduli at different frequencies. This is of interest in a similar analogy to ionic hydraulic actuators [15]. Obviously, water leakage is a definite disadvantage in achieving high efficiency for the IPMC. This issue should be resolved to obtain much higher efficiencies and specific power for the IPMCs as actuators and sensors.

5. Methodology to achieve high-force-density IPMCs

As discussed earlier, a key engineering problem in achieving high-force-density IPMCs is reducing or eliminating the water leakage out of the surface electrode (made of finely dispersed platinum particles within the near-boundary region) so that water transport within the IPMC can be more effectively utilized for actuation. Figure 7 depicts that the nominal size of platinum particles in the IPMC near the boundary is ca 40–60 nm, that is much larger than that (∼5 nm) of incipient particles associated with ion clusters [10]. Thus, the incipient particles coagulate during the chemical reduction process and eventually grow large as schematically illustrated in figure 16. One can then realize that there is a significant potential for controlling this process in terms of platinum particle penetration, size and distribution. This could be achieved by introducing effective dispersing agents (additives) during the chemical reduction process. One can anticipate that the additives should enhance dispersal of platinum particles within the ionic polymer and thus reduce coagulation. As a result, a better platinum particle penetration in the polymer with a smaller average particle size and more uniform distribution could be obtained. This uniform distribution makes it more difficult for water to pass through (granular damming effect). Thus, the water leakage out of the surface electrode could be significantly reduced.

The use of effective dispersing agents during the platinum metallization process has recently resulted in dramatically improved force density characteristics. The results are shown in figure 17, where the measured force of the improved IPMC relative to the conventional one is reported. As clearly seen, the additive treaded IPMC shows

(i) a much sharper response to the input electric field and
(ii) a dramatically increased force density generation by as much as 100%.

One key observation is the virtual disappearance of the delayed response, which has been observed in the conventional IPMCs. Such an effect can be translated into a higher-power IPMC than any other IPMCs reported so far.

In figure 18, a SEM micrograph along with its x-ray line-scan is provided. As can be seen, a good platinum penetration is achieved meaning that an effective additive enhances platinum dispersion leading to better penetration in the polymer. A convenient way to handle this situation (free diffusion into finite porous slab or membrane) is to use an effective diffusivity, D_{eff}, and, then, to consider it as a one-dimensional problem. Assuming fast kinetics for the metal precipitation reaction of $[Pt(NH_3)_4]^{2+} + 2e^- \Rightarrow Pt^o + 4NH_3$, the precipitated platinum concentration, N_x, can be expressed as

$$N_x = \frac{C_{\text{Pt}}(\delta_i)}{C_{\text{Pt},i}} = 1 - \text{erf}\left(\frac{\delta_t}{\sqrt{4D_{\text{eff}}t}}\right), \qquad (7)$$

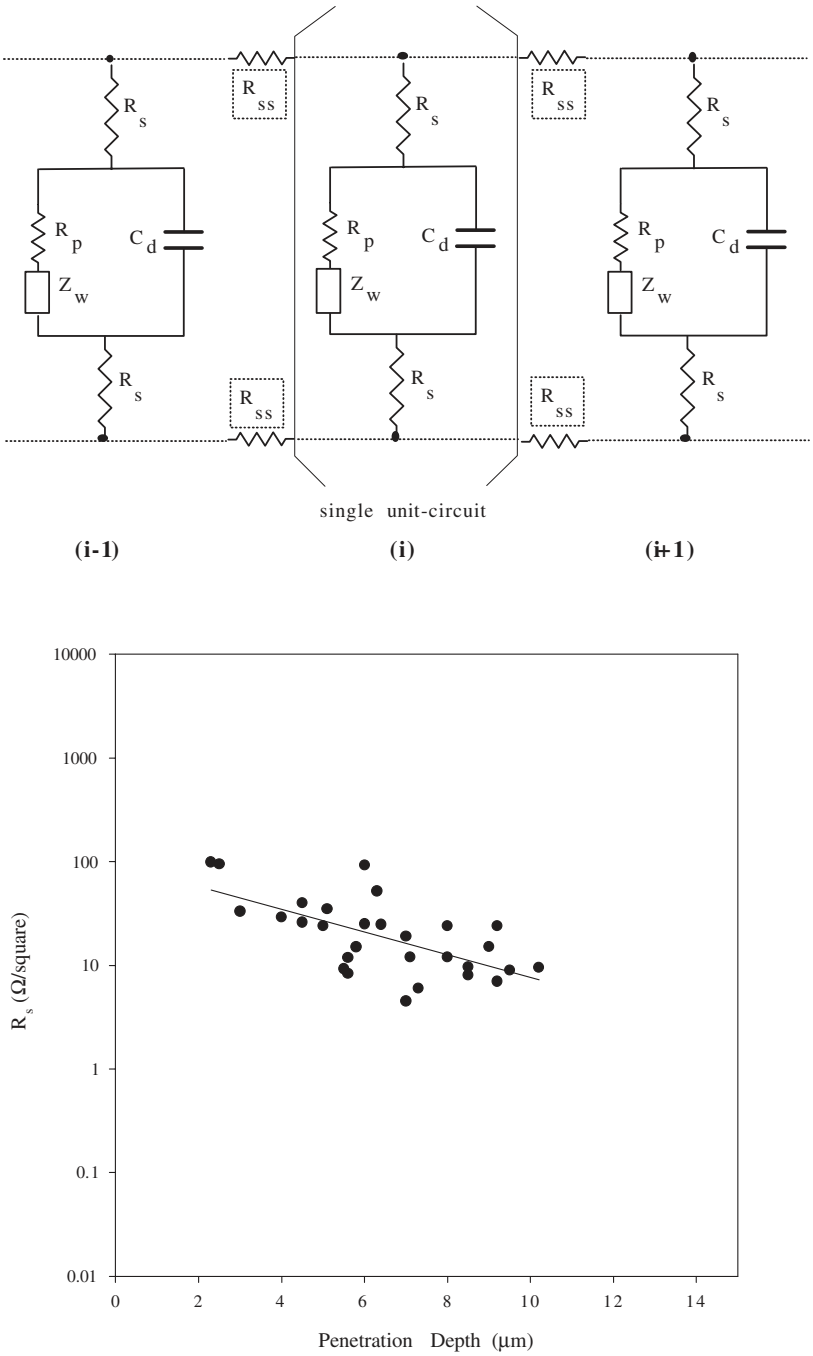

Figure 12. A possible equivalent electric circuit of a typical IPMC membrane (top) and measured surface resistance, R_s, as a function of platinum penetration depth (bottom). Note that SEM was used to estimate the penetration depth of platinum in the membrane. The four-probe method was used to measure the surface resistance, R_s, of the IPMCs. Clearly, the deeper the penetration, the lower the surface resistance is.

where notations $C_{Pt}(\delta_t)$, $C_{Pt,i}$ and δ_t are the platinum concentration, the platinum concentration at the interface and the particle penetration depth, respectively. For a typical reduction time of $t = 15$ min (in figure 18), equation (7) is plotted for values of $D_{eff} = 1 \times 10^{-10}$, 1×10^{-9} and 1×10^{-8} cm^2 s^{-1}, respectively. The effective diffusivity, D_{eff}, could be estimated to be of the order of 1×10^{-8} cm^2 s^{-1} for the improved IPMC. Although this situation is somewhat complicated due to the simultaneous effect of a mass transfer and significant kinetics, nevertheless, the estimated value of $D_{eff} \sim 1 \times 10^{-8}$ cm^2 s^{-1} would be a convenient value for engineering design of the platinum metallization process described here for the improved IPMC.

In figure 19, the results of potentiostatic analysis are presented. The variation of current following the application of an electric potential to the IPMCs (both the PVP-treated IPMC and the conventional IPMC) is shown. The current decays exponentially. The charge transfer after time t (Q_t) is $Q_t = \int_0^t I_t \, dt$. It is useful to make a direct comparison between $Q_{t,PVP}$ (for the PVP-treated IPMC) and Q_t (for

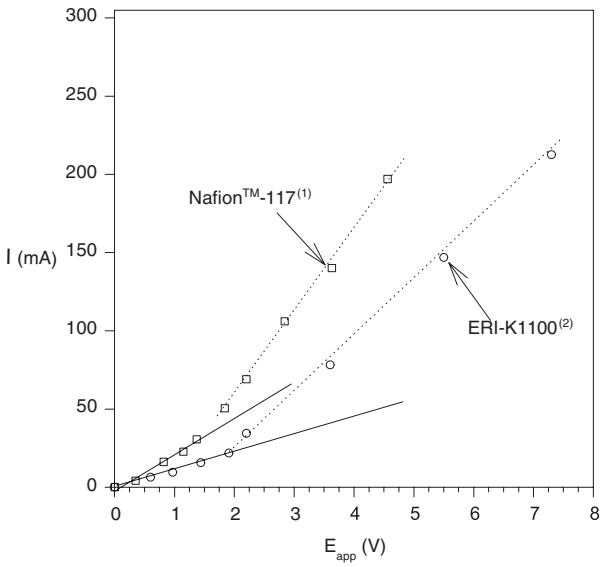

Figure 13. Steady-state current, I, versus applied voltage, E_{app}, on typical IPMCs. ERI-K1100 stands for a proprietary IPMC fabricated by Environmental Robots, Inc—it has a thickness of 2.9 mm and is suitably platinum/gold electroded.

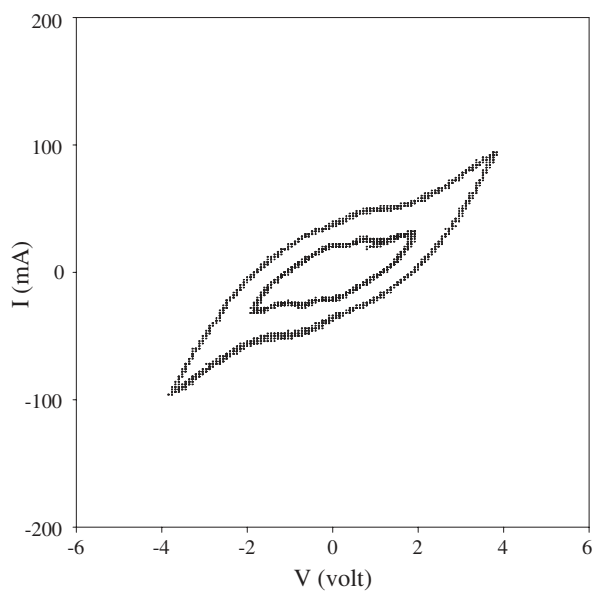

Figure 14. I/V curves for a typical IPMC (Nafion™-117-based IPMC). Note that the scan rate is 100 mV s^{-1}. A simple behaviour with a small hysteresis can be seen. It does not show any distinct reduction or re-oxidation peaks within ±4 V, except for a decomposition behaviour at ∼ ±1.5 V, where the extra current consumption is apparent due to electrolysis.

the conventional IPMC). The data shown in figure 19 give $Q_{t,\text{PVP}}/Q_t \cong 1.1$. This means that the PVP-treated IMPC consumes approximately 10% more charges. This raises a concern that only a 10% increased consumption of charges is not the only reason to increase the force density by as much as 100%. Therefore, it can be concluded that the 'granular damming effect' that minimizes the water leakage out of the porous surface electrode region, when the IPMC strip bends, plays an important role.

High-force-density IPMC—a view from linear irreversible thermodynamics. In connection with the phenomenological laws and irreversible thermodynamics considerations previously discussed in section 3, when one considers the actuation with ideal impermeable electrodes, which results in $Q = 0$ from equation (3), one has

$$\nabla p = \frac{L}{K}\vec{E}. \tag{8}$$

Also, the pressure gradient can be estimated from

$$\nabla p \cong \frac{2\sigma_{\max}}{h}, \tag{9}$$

where $\sigma_{\max}$ and h are the maximum stress generated under an imposed electric field and the thickness of the IPMC, respectively. The values of $\sigma_{\max}$ can be obtained when the maximum force (= blocking force) is measured at the tip of the IPMC for a given electric potential. In figure 20, the maximum stresses generated, $\sigma_{\max}$, under an imposed electric potential, E_0, for both calculated values and experimental values of the conventional IPMC and the improved IPMC are presented. It should be noted that the improved IPMC (by the method of using additives) is superior to the conventional IPMC, approaching the theoretically obtained values.

High-force-density IPMC—thermodynamic efficiency The bending force of the IPMC is generated by the effective redistribution of hydrated ions and water. This is an ion-induced hydraulic actuation phenomenon. Typically, such a bending force is electric-field-dependently distributed along the length of the IPMC strip as noted in figure 12. Further, note from figure 12 that a surface voltage drop occurs, which can be minimized [6]. The IPMC strip bends due to these ion migration-induced hydraulic actuation and redistribution. The total bending force, F_t, can be approximated as

$$F_t \cong \int_0^L f \, \mathrm{d}L, \tag{10}$$

where f is the force density per unit length. Assuming a uniformly distributed load over the length of the IPMC, the mechanical power produced by the IPMC can be estimated from

$$P_{\text{out}} = F_t v. \tag{11}$$

Notation v is the average tip velocity of the IPMC in action. Finally, the thermodynamic efficiency, $E_{\text{ff,em}}$, can be obtained as

$$E_{\text{ff,em}}\ (\%) = \frac{P_{\text{out}}}{P_{\text{in}}} \times 100, \tag{12}$$

where P_{in} is the electrical power input to the IPMC. Based on equation (12), one can construct a graph (see figure 21) which depicts the thermodynamic efficiency of the IPMC as a function of frequency. Note that this graph presents the experimental results for the conventional IPMC and the improved additive-treated IPMC. It is of note that the optimum efficiencies occur near 5–10 Hz for these IPMCs. The optimum values of these IPMCs are approximately 2.5–3.0%. At low frequencies, the water leakage out of the surface electrode seems to reduce the efficiency significantly. However, the

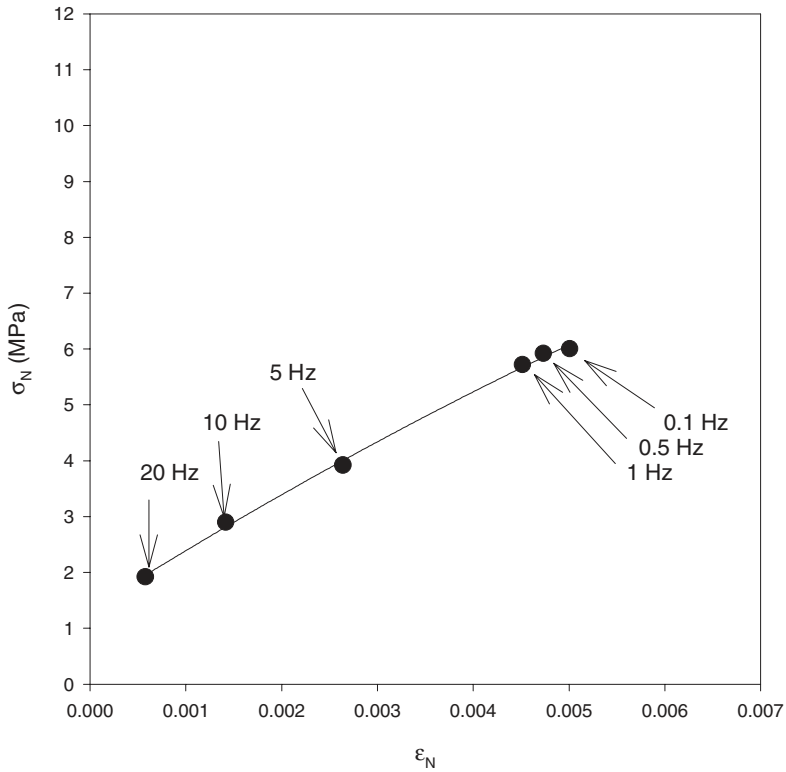

Figure 15. Frequency dependence of the IPMC in terms of the normal stress, σ_N, versus the normal strain, ε_N, under an imposed step voltage of 1 V. (This Nafion^{TM}-117 IPMC has a cation of Li^+ and a size of 5 × 20 mm.)

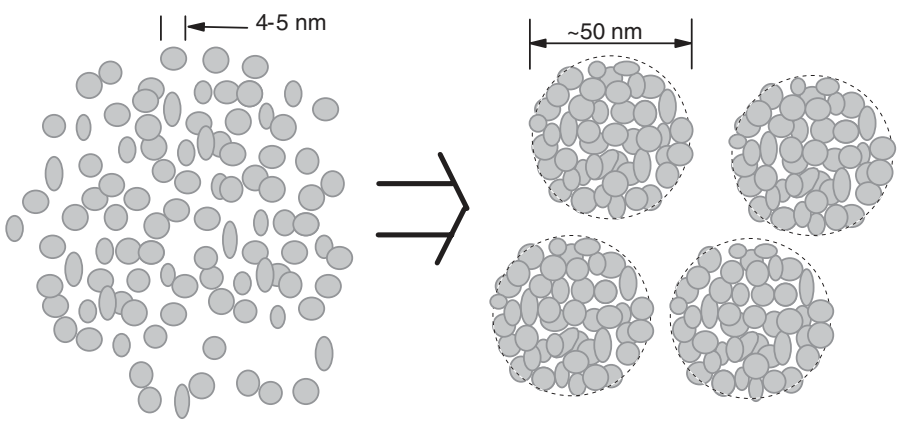

Figure 16. A schematic illustration of platinum coagulation during the chemical reduction process.

additive-treated IPMC shows a dramatic improvement in efficiency due to reduction in water leakage out of the electrode surface. The important sources of energy consumption for the IPMC actuation could be from

(i) the necessary mechanical energy needed to cause the positive/negative strains for the IPMC strip,
(ii) the I/V hysteresis due to the diffusional water transport within the IPMC,
(iii) the thermal losses—Joule heating (see figure 22),
(iv) the decomposition due to water electrolysis and
(v) the water leakage out of the electrode surfaces.

Despite our effort to improve the performance of the IPMC by blocking water leakage out of the porous surface electrode, the overall thermodynamic efficiencies of all IPMC samples tested in a frequency range of 0.1–10 Hz remain somewhat low. However, it should be noted that the obtained values are favourable compared to other types of bending actuator, i.e. conducting polymers and piezoelectric materials at similar conditions, exhibiting considerably lower efficiencies [13, 14].

Figure 22 displays IR thermographs taken for an IPMC in action (the sample size of 1.2 × 7.0 cm). They show spectacular multi-species mass/heat transfer in a samples of IPMC under an oscillatory step voltage of 3 V and frequency of 0.1 Hz. The temperature difference is more than 10 °C. In general, the hot spot starts from the electrode and propagates toward the tip of the IPMC strip (left to right). The thermal propagation is simultaneously conjugated with the mass transfer along with

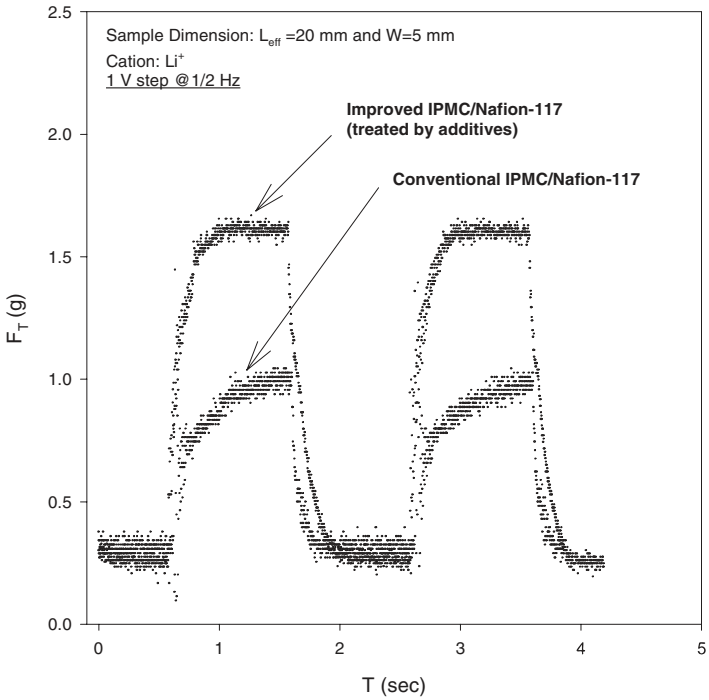

Figure 17. Force response characteristics of the improved IPMC versus the conventional IPMC. Note that the improved IPMC is one treated by an effective additive.

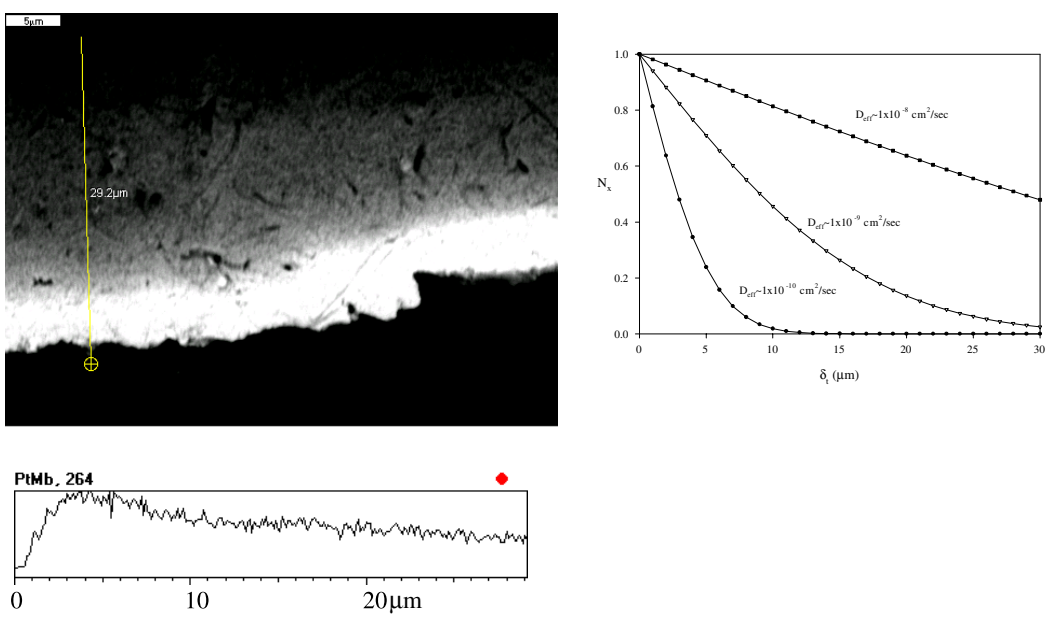

Figure 18. An SEM micrograph of an IPMC treated with a dispersing agent (top left) and its x-ray line-scan (bottom left) and platinum penetration profiles (right). As can be seen, the Pt penetration is greater and consistent.

the possible electrochemical reactions. It clearly shows the significance of water transport within the IPMC. These coupled transport phenomena are currently under investigation.

6. Conclusions

In this review paper, the first in a series of four review papers, the fundamental properties and characteristics of IPMCs as biomimetic sensors, actuators and artificial muscles have been briefly presented. This paper presented a summary of all recent findings and current state-of-the art manufacturing techniques, governing phenomenological laws and the mechanical and electrical characteristics. A number of recent breakthroughs in developing high-force-density IPMCs were also reported.

It was established that the successful commercialization of the IPMC is highly dependent upon further improvement of its thermodynamic efficiency and force density generation. In particular, the dimensional scale-up of the IPMC is a major factor enhancing its useful forces. The ultimate goal of using IPMCs as soft biomimetic sensors and actuators can

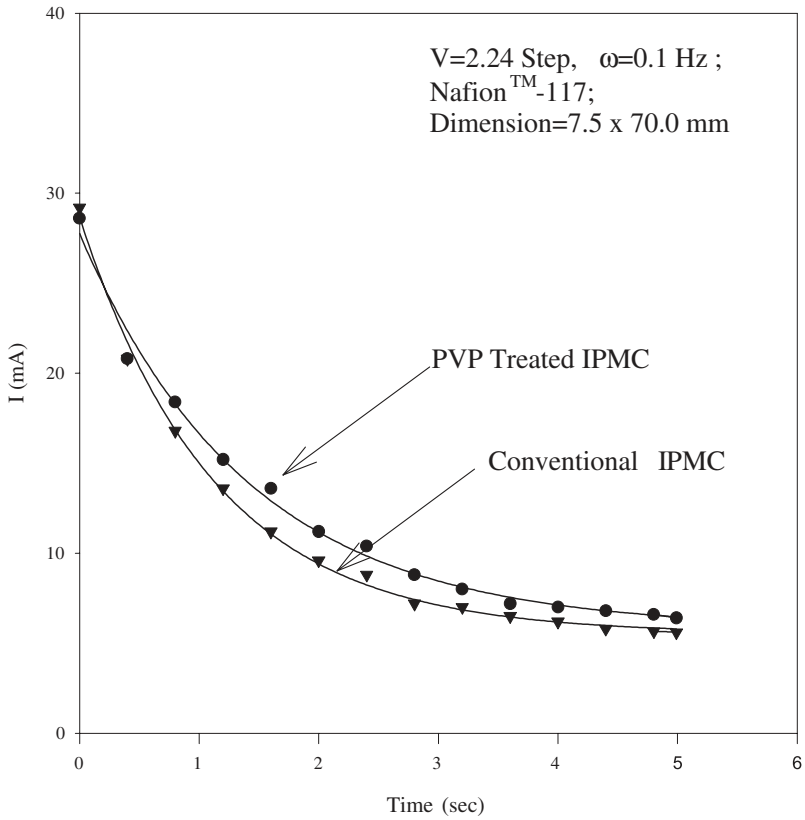

Figure 19. Potentiostatic Coulometric analysis for the additive-treated IPMC and the conventional IPMC. This graph shows that an increased current passage (Faraday approach) can contribute to the observed improvement in the force characteristics of IPMC strips (see figure 17).

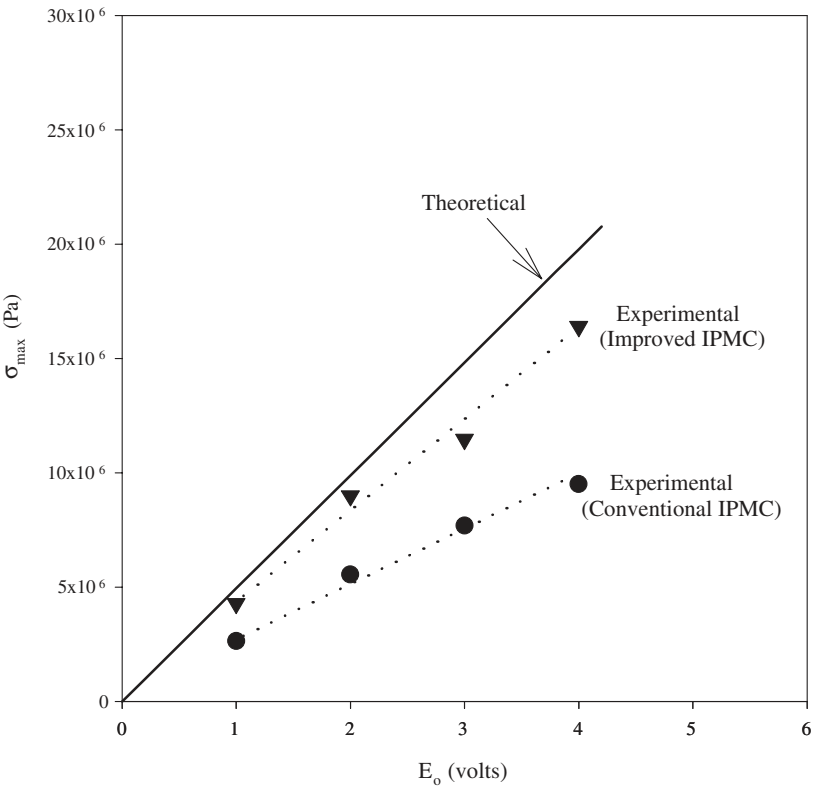

Figure 20. Maximum stresses generated by the IPMCs at given voltages. For theoretical calculation the following experimentally measured values were used: (*a*) $L_{12} = L_{21} = 2 \times 10^{-8}$ (cross-coefficient, (m s^{-1})/(V m^{-1})) (*b*) $k = 1.8 \times 10^{-18}$ (hydraulic permeability, m^2 [12]), and (*c*) $\vec{E} = E_0/h$, where $h = 200$ μm (membrane thickness).

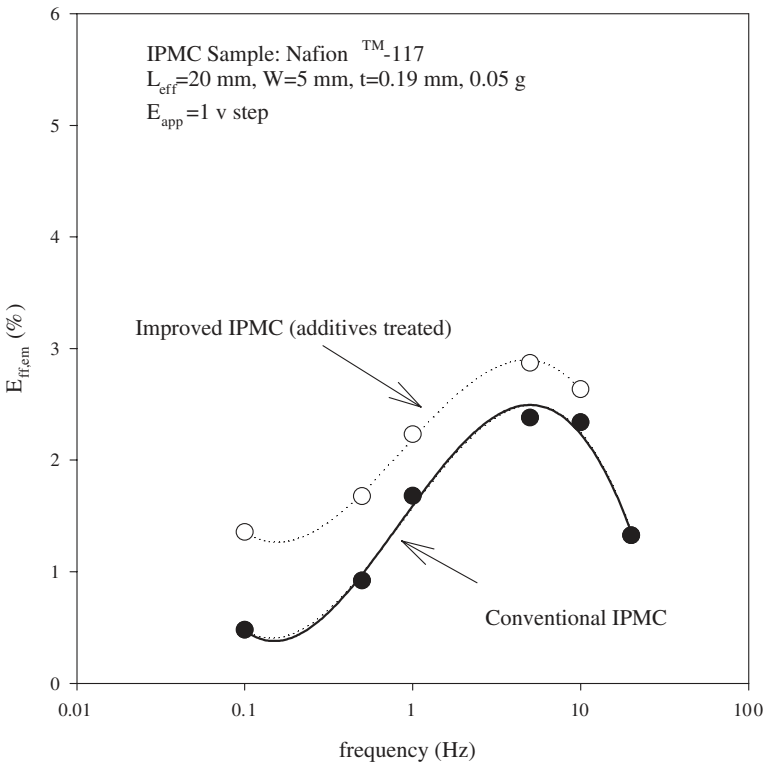

Figure 21. Thermodynamic efficiency of the IPMC as a function of frequency.

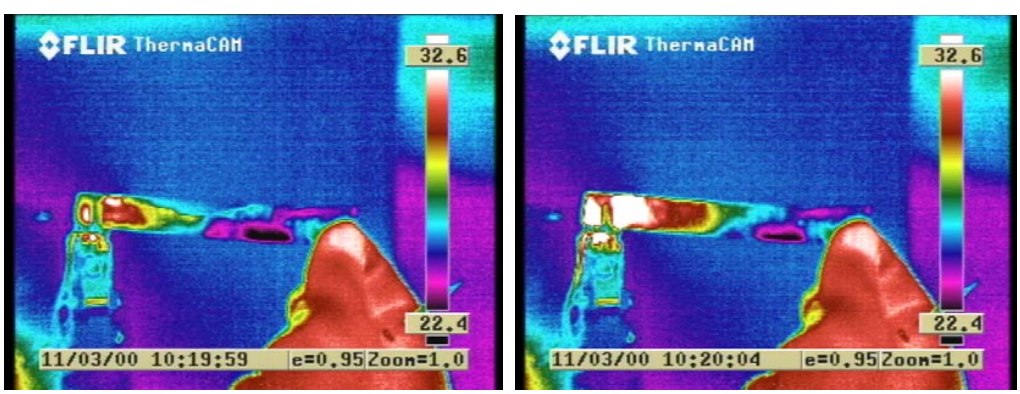

t= 0 sec; t= 5 sec;

Figure 22. IR thermographs taken for an IPMC in action. The hot stop starts from the electrode and propagates toward the tip of the IPMC strip. The electrode is positioned on the left side of the IPMC. The temperature difference is more than 10 °C when a dc voltage of 3 V is applied for the IPMC sample size of 1.2 × 7.0 cm.

be clearly envisioned upon the successful development of three-dimensional systems of IPMCs to be used as electrically controllable/deformable three-dimensional smart structures. In future communications, we will discuss our effort to achieve these challenges.

Acknowledgments

This work was partially supported by US NRL/DARPA. The authors thank the technical staff of Environmental Robots, Inc. and the Artificial Muscle Research Institute of the University of New Mexico for the laboratory work. Discussions with Professor P G de Gennes of the College de France are also gratefully acknowledged.

References

[1] Oguro K, Asaka K and Takenaka H 1993 Actuator element *US Patent Specification* 5 268 082
[2] Asada A, Oguro K, Nishimura Y, Misuhata M and Takenaka H 1995 Bending of polyelectrolyte membrane–platinum composites by electric stimuli, I. Response characteristics to various wave forms *Polym. J.* **27** 436–40
[3] Shahinpoor M, Adolf D, Segalman D and Witkowski W 1993

Electrically controlled polymeric gel actuators *US Patent Specification* 5 250 167
[4] Shahinpoor M and Mojarrad M 2000 Soft actuators and artificial muscles *US Patent Specification* 6 109 852
[5] Shahinpoor M, Bar-Cohen Y, Simpon J O and Smith J 1998 Ionic polymer–metal composites (IPMC) as biomimetic sensors and structures—a review *Smart Mater. Struct.* **7** 15–30
[6] Shahinpoor M and Kim K J 2000 The effect of surface-electrode resistance on the performance of ionic polymer–metal composites (IPMC) artificial muscles *Smart Mater. Struct.* **9** 543–51
[7] de Gennes P G, Okumura K, Shahinpoor M and Kim K J 2000 Mechanoelectric effects in ionic gels *Europhys. Lett.* **50** 513–8
[8] Takenaka H, Torikai E, Kwami Y and Wakabayshi N 1982 Solid polymer electrolyte water electrolysis *Int. J. Hydrog. Energy* **7** 397–403
[9] Millet P, Pineri M and Durand R 1989 New solid polymer electrolyte composites for water electrolysis *J. Appl. Electrochem.* **19** 162–6
[10] Kim K J, Shahinpoor M and Razani A 2000 Preparation of IPMCs for use in fuel cells, electrolysis, and hydrogen sensors *Proc. SPIE 7th Int. Symp. on Smart Structures and Materials* vol 3687 pp 110–20
[11] Peace G S 1993 *Taguchi Methods: Hands-On Approach* (New York: Addison-Wesley)
[12] Bernardi D M and Verbrugge M W 1992 A mathematical model of the solid-polymer-electrolyte fuel cell *J. Electrochem. Soc.* **139** 2477–91
[13] Wang Q, Du X, Xu B and Cross L E 1999 Electromechanical coupling and output efficiency of piesoelectric bending actuators *IEEE Trans. Ultrason. Ferroelectr. Freq. Control* **46** 638–46
[14] Pei Q, Inganas O and Lundstrom I 1993 Bending bilayer strips built from polyaniline for artificial electrochemical muscles *Smart Mater. Struct.* **2** 1–5
[15] Shahinpoor M and Kim K J 2001 Novel ionic polymeric hydraulic actuators *Proc. SPIE 8th Annu. Int. Symp. on Smart Structures and Materials (Newport Beach, CA, 2001)* SPIE Publication No 4329–3